The Astrophysical Journal Letters, 982:L26 (8pp), 2025 March 20 https://doi.org/10.3847/2041-8213/adb83d

A Massive H I-absorption-selected Galaxy at $z \approx 2.356$

B. Kaur[1,2], N. Kanekar[1], M. Neeleman[3], Y. Zhu[4], J. X. Prochaska[5,6], M. Rafelski[7,8], and G. Becker[9]
[1] National Centre for Radio Astrophysics, Tata Institute of Fundamental Research, Pune University, Pune 411007, India; bkaur@ncra.tifr.res.in
[2] Inter-University Centre for Astronomy and Astrophysics, Pune University, Pune 411007, India
[3] National Radio Astronomy Observatory, 520 Edgemont Road, Charlottesville, VA 22903, USA
[4] Steward Observatory, University of Arizona, 933 N Cherry Ave, Tucson, AZ 85721, USA
[5] Department of Astronomy & Astrophysics, UCO/Lick Observatory, University of California, 1156 High Street, Santa Cruz, CA 95064, USA
[6] Kavli Institute for the Physics and Mathematics of the Universe (Kavli IPMU), 5-1-5 Kashiwanoha, Kashiwa, 277-8583, Japan
[7] Space Telescope Science Institute, 3700 San Martin Drive, Baltimore, MD 21218, USA
[8] Department of Physics & Astronomy, Johns Hopkins University, Baltimore, MD 21218, USA
[9] University of California, Riverside, 900 University Ave, Riverside, CA 92521, USA
Received 2025 January 6; revised 2025 February 8; accepted 2025 February 19; published 2025 March 19

Abstract

We use the Karl G. Jansky Very Large Array (VLA) and the Atacama Large Millimeter/submillimeter Array to detect CO(1–0), CO(3–2), and rest-frame 349 GHz continuum emission from an H I-selected galaxy, DLA1020+2733g, at $z \approx 2.3568$ in the field of the $z = 2.3553$ damped Lyα absorber (DLA) toward QSO J1020+2733. The VLA CO(1–0) detection yields a molecular gas mass of $(2.84 \pm 0.42) \times 10^{11} \times (\alpha_{\rm CO}/4.36)\, M_\odot$, the largest ever measured in an H I-selected galaxy. The DLA metallicity is $+0.28 \pm 0.16$, from the Zn IIλ2026 absorption line detected in a Keck Echellette Spectrograph and Imager spectrum. This continues the trend of high-metallicity DLAs being frequently associated with massive galaxies. We obtain a star formation rate (SFR) of $\lesssim$400 $M_\odot$ yr^{-1} from the rest-frame 349 GHz continuum emission and a relatively long molecular gas depletion timescale of $\gtrsim$0.6 Gyr. The excitation of the $J = 3$ rotational level is subthermal, with $r_{31} \equiv L'_{\rm CO(3-2)}/L'_{\rm CO(1-0)} = 0.513 \pm 0.081$, suggesting that DLA1020+2733g has a low SFR surface density. The large velocity spread of the CO lines, $\approx$500 km s^{-1}, and the long molecular gas depletion timescale suggest that DLA1020+2733g is likely to be a cold rotating-disk galaxy.

Unified Astronomy Thesaurus concepts: Damped Lyα systems (349); Radio interferometry (1346); High-redshift galaxies (734)

1. Introduction

The presence of a damped Lyα absorber (DLA; with H I column density $\geqslant 2 \times 10^{20}$ cm^{-2}) in a QSO absorption spectrum has long been used as a signpost of the presence of a galaxy close to or along the QSO sight line (e.g., A. M. Wolfe et al. 1986, 2005). Numerous studies have tried to identify these galaxies at high redshifts over the last three decades (e.g., V. P. Kulkarni et al. 2000; P. Møller et al. 2004; J. P. U. Fynbo et al. 2010; C. Péroux et al. 2012; M. Fumagalli et al. 2014; W.-H. Wang et al. 2015; J. K. Krogager et al. 2017). Such galaxy samples, selected by their H I absorption, are not biased toward objects with high luminosity or star formation activity and thus offer a view of the high-redshift Universe complementary to that provided by the usual galaxy populations identified by their stellar emission in deep optical or near-infrared images (e.g., P. Madau & M. Dickinson 2014). Characterizing such high-z H I-absorption-selected galaxies and connecting them to the emission-selected population have hence long been of much interest (e.g., P. Møller et al. 2002; A. M. Wolfe et al. 2005; B. Kaur et al. 2021; N. H. P. Rhodin et al. 2021). QSO absorption spectra also provide detailed information on the element abundance, gas-phase metallicity, molecular fraction, and gas temperature, etc., along the DLA sight line (e.g., P. Noterdaeme et al. 2008; N. Kanekar et al. 2014; M. Rafelski et al. 2014; M. Neeleman et al. 2015; A. De Cia et al. 2016; S. A. Balashev et al. 2019). This allows one to connect the properties of absorption-selected galaxies to the properties of their interstellar and circumgalactic mediums (CGMs), not usually possible with other high-z galaxy samples.

Unfortunately, despite many efforts, the presence of the nearby bright background QSO has made it difficult to even identify, let alone characterize, high-z DLA galaxies via their stellar or nebular emission. Only a few tens of DLA galaxies have been identified out to $z \approx 3$ by such approaches today (e.g., J. K. Krogager et al. 2017; E. K. Lofthouse et al. 2023; G. A. Oyarzún et al. 2024), with biases implicit in the observational technique (e.g., against dusty galaxies and galaxies at high-impact parameters; e.g., G. A. Oyarzún et al. 2024).

The advent of the Atacama Large Millimeter/submillimeter Array (ALMA) has changed the field, opening two new windows, via the [C II] 158 μm fine-structure line and the CO rotational lines, on high-z DLA galaxies (e.g., M. Neeleman et al. 2017, 2018, 2019; P. Møller et al. 2018; N. Kanekar et al. 2018, 2020; A. Klitsch et al. 2019; C. Péroux et al. 2019). ALMA [C II] 158 μm searches in the fields of DLAs at $z \approx 4$ have yielded the first identifications of H I-selected galaxies at such high redshifts (M. Neeleman et al. 2017, 2019; M. Neeleman et al. 2025. Remarkably, the identified DLA galaxies at $z \gtrsim 4$ are at relatively high impact parameters, $\approx$15–60 kpc, with no evidence of a galaxy closer to the QSO sight line (e.g., M. Neeleman et al. 2019, 2025; B. Kaur et al. 2021). This indicates that high H I column densities are prevalent in the CGM of typical galaxies at $z \approx 4$. Higher-resolution ALMA [C II] 158 μm mapping of two of these galaxies has resulted in the identification of the first cold, rotating-disk galaxy, the "Wolfe disk," at $z > 4$ (M. Neeleman et al. 2020) and a pair of merging galaxies at $z \approx 3.8$ (J. X. Prochaska et al. 2019). Follow-up Hubble Space Telescope

imaging has yielded the detection of the rest-frame near-ultraviolet stellar emission from a number of DLA galaxies at $z \approx 4$, while Karl G. Jansky Very Large Array (VLA) CO studies have measured, or placed limits on, their molecular gas mass (M. Neeleman et al. 2020; B. Kaur et al. 2021).

At somewhat lower redshifts, $z \approx 2$–3, ALMA, and Northern Extended Millimetre Array (NOEMA) searches for redshifted CO emission have identified approximately 7 H I-selected galaxies in DLA fields (e.g., J. P. U. Fynbo et al. 2018; M. Neeleman et al. 2018; N. Kanekar et al. 2020; B. Kaur et al. 2022b; F. Combes & N. Gupta 2024). While such CO studies are only sensitive to galaxies with a high molecular gas mass, it is remarkable that many high-metallicity DLAs, with [M/H] $\gtrsim -0.3$, are associated with massive galaxies, with molecular gas mass $\gtrsim 5 \times 10^{10}\,M_{\odot}$ (N. Kanekar et al. 2020; B. Kaur et al. 2022a). Evidence has been found for a dependence of both the [C II] 158 μm detection rate at $z \approx 4$ and the CO detection rate at $z \approx 2$ on DLA metallicity, with higher-metallicity DLAs at each redshift yielding a significantly higher detection rate of galaxies in the DLA field. Recently, B. Kaur et al. (2024) carried out the first CO mapping of a high-z H I-selected galaxy, finding evidence that the $z \approx 2.193$ DLA toward PKS B1228-113 also arises in a massive, cold, dusty rotating disk.

Only ≈20 DLA fields have so far been searched for redshifted CO emission at $z \approx 2$ (N. Kanekar et al. 2020; B. Kaur et al. 2022b). The efficiency of such searches can be significantly increased by targeting sight lines containing multiple DLAs, such that multiple DLA redshifts can be simultaneously searched for CO emission. We have begun such a program to use ALMA, NOEMA, and the VLA to search for redshifted CO emission from such "double-DLA" fields at $z \approx 2$. Here, we report the ALMA and VLA detection of redshifted CO emission from an ultramassive H I-selected galaxy at $z \approx 2.356$, from the double-DLA field toward QSO J1020+2733.[10]

2. Observations and Data Analysis

The sight line toward QSO J1020+2733 (at $z = 2.712$) was identified as containing two DLAs at redshifts of $z \approx 2.36$ and $z \approx 2.29$ in a Sloan Digital Sky Survey (SDSS) spectrum (L. Mas-Ribas et al. 2017; A. Arinyo-i-Prats et al. 2018). The redshifted CO lines of both DLAs were simultaneously covered in the ALMA CO(3–2) and VLA CO(1–0) observations. We also used the Echellette Spectrograph and Imager (ESI; A. I. Sheinis et al. 2002) on board the Keck II Telescope to obtain an optical spectrum of QSO J1020+2733 to accurately measure the metallicities of the two putative DLAs. Finally, we reanalyzed the SDSS spectrum of QSO J1020+2733 to provide updated H I column densities of the two absorbers, based on the more accurate redshift information from the metal lines detected in the ESI spectrum.

2.1. VLA Observations and Data Analysis

The VLA observations (proposal ID: VLA/23B-286; PI: N. Kanekar) were carried out on 2023 December 30 and 31, using the *Ka*-band receivers in the D-configuration, with a total on-source time of ≈3 hr. The WIDAR correlator was set up in 8 bit mode, with two 1 GHz intermediate frequency (IF) bands, each divided into eight 128 MHz digital subbands. Two of the subbands were centered at the redshifted CO(1–0) line frequencies for the DLA redshifts (35.06 GHz and 34.34 GHz), with 256 channels, a velocity resolution of ≈4.3 km s^{-1}, and a velocity coverage of ≈1100 km s^{-1}. The remaining subbands were placed at contiguous frequencies, covering the frequency range 34.62–35.64 GHz, with a velocity resolution of ≈8.5 km s^{-1}.

The VLA data were analyzed following standard procedures in the Common Astronomy Software Application (CASA version 5.6.1.8; CASA Team 2022). After initial data editing, the tasks GAINCALR and BANDPASSR from the CALR package[11] were used to measure the antenna-based gains and bandpasses for each observing run. These were applied to the multichannel visibility data, and the calibrated target visibilities from the two runs were then split out and combined together into a single data set. The spectral windows containing the two redshifted CO(1–0) line frequencies were then imaged using the task TCLEAN, with natural weighting and a velocity resolution of 50 km s^{-1}, to obtain the final spectral cubes with an angular resolution of ≈3.″0 × 2.″4. The cubes were cleaned down to a flux density threshold of 0.5σ, using a mask of size ≈12″ × 12″ that encloses all the CO(1–0) emission, where $\sigma \approx 0.14$ mJy Beam^{-1} is the rms noise per 50 km s^{-1} channel on the cubes.

2.2. ALMA Observations and Data Analysis

The ALMA observations (proposal ID: 2023.1.01415; PI: J. X. Prochaska) were carried out on 2024 March 12 using 45 ALMA antennas in the C43-1 configuration, the Band-3 receivers, and a total on-source time of ≈48 m. The ALMA correlator was set up in 4 bit Frequency Division Mode (FDM) for the three IF bands, covering the redshifted CO(3–2) line frequency for $z = 2.2876$ and $z = 2.3564$ (i.e., frequencies of ≈105.18 GHz and ≈103.03 GHz, respectively), and in Time Division Mode (TDM) for the fourth band, used to cover the continuum emission. The three FDM bands each had a bandwidth of 937.5 MHz, subdivided into 120 channels, i.e., a velocity coverage of ≈2700 km s^{-1} and a velocity resolution of ≈22.5 km s^{-1}, at the redshifted CO(3–2) line frequencies, while the TDM band used a bandwidth of 2 GHz and 128 channels.

The initial data editing and calibration of the ALMA data used the standard ALMA pipeline in the CASA package (version 6.5.4.9; CASA Team 2022; T. R. Hunter et al. 2023). We then used manual flagging to remove outliers in the calibrated visibilities before averaging the data to a coarse spectral resolution for the purpose of continuum imaging. The imaging used Briggs weighting (D. S. Briggs 1995) with a robust value of +1, yielding a synthesized beam of 3.″7 × 3.″2 and an rms noise of 27 μJy Beam^{-1} on the 104 GHz continuum image. We then used the task UVSUB to subtract out the continuum emission from the calibrated visibilities. Finally, we used the task TCLEAN to make spectral cubes for the IF bands covering the redshifted CO(3–2) emission from the two DLA redshifts, using Briggs weighting with a robust value of +1 and a velocity resolution of 23 km s^{-1}. The cubes were cleaned down to a flux density threshold of 0.5σ, using a mask of size ≈15″ × 15″ centered on the CO emission, where $\sigma = 0.37$ mJy Beam^{-1}. The angular resolution of the spectral cubes is ≈3.″7 × 3.″1.

[10] We use a flat Λ cold dark matter cosmology, with $\Omega_{\Lambda} = 0.7$, $\Omega_m = 0.3$, and $H_0 = 70$ km s^{-1} Mpc^{-1}, throughout the Letter.

[11] The CalR package is publicly available at https://github.com/chowdhuryaditya/calR (A. Chowdhury et al. 2020, 2022; A. Chowdhury 2021).

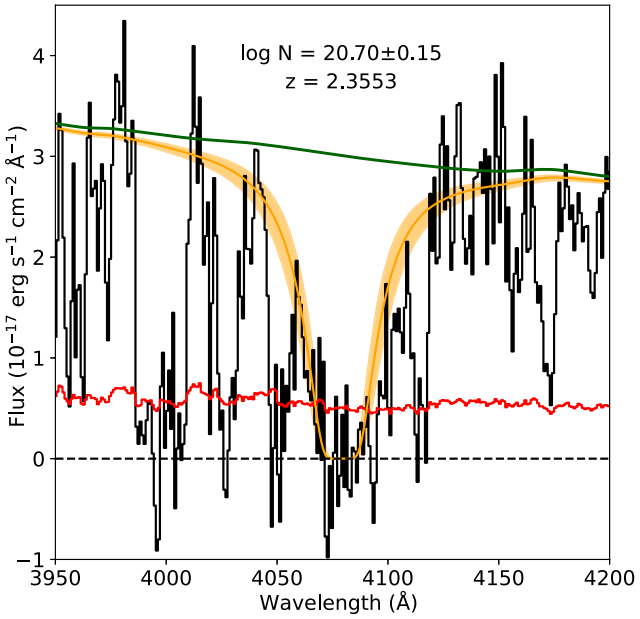

Figure 1. The SDSS spectrum of QSO J1020+2733 centered on the Lyα absorption feature at $z = 2.3553$. The green line is the continuum fit to the quasar spectrum obtained with the python package *linetools*. The orange line is a fit to the Lyα absorption profile at $z = 2.3553$, while the orange-shaded region shows the 1σ uncertainty on the fit. The 1σ uncertainty on the spectrum is shown in red. The spectrum also shows saturated Lyα absorption at $z = 2.2876$ (≈4000 Å).

2.3. Keck ESI Observations and Data Analysis

QSO J1020+2733 was observed on 2024 June 1 using ESI on the Keck II telescope in echellette mode, with a 1″ slit and a total exposure time of 1200 s. The data were analyzed following the reduction procedures outlined in G. D. Becker et al. (2019) using a custom pipeline. This pipeline includes optimal sky subtraction techniques (D. D. Kelson 2003), 1D spectral extraction (K. Horne 1986), and telluric absorption corrections, which were based on atmospheric models from the Cerro Paranal Advanced Sky Model (S. Noll et al. 2012; A. Jones et al. 2013). The spectra were extracted with a pixel size of 15 km s^{-1}; the typical velocity resolution is approximately 45 km s^{-1} (FWHM), and the S/N per pixel redward of the Lyα emission line of the quasar is ≈10.

3. Results

Our Keck ESI spectrum of QSO J1020+2733 revealed a slew of metal lines at $z = 2.3553$, but no strong metal absorption was seen at the redshift of the second SDSS DLA at $z = 2.2876$. While saturated Lyα absorption is indeed seen at $z = 2.2876$ in the SDSS spectrum of QSO J1020+2733, there is no evidence of damping wings. This absorber is thus likely to be a blend of Lyman-limit systems and not a DLA, and we will not discuss it further here.

Figure 1 shows a zoom-in on the damped Lyα absorption detected at $z = 2.3553$ toward QSO J1020+2733 in the SDSS spectrum.[12] The solid orange curve shows our fit to the damped Lyα profile, while the orange-shaded region shows the 1σ uncertainty on the fit. From the fit to the H I absorption profile,

[12] We note that the DLA lies at the extreme blue end of the ESI spectrum, where the S/N is very low; we have hence measured the HI column density from the SDSS spectrum.

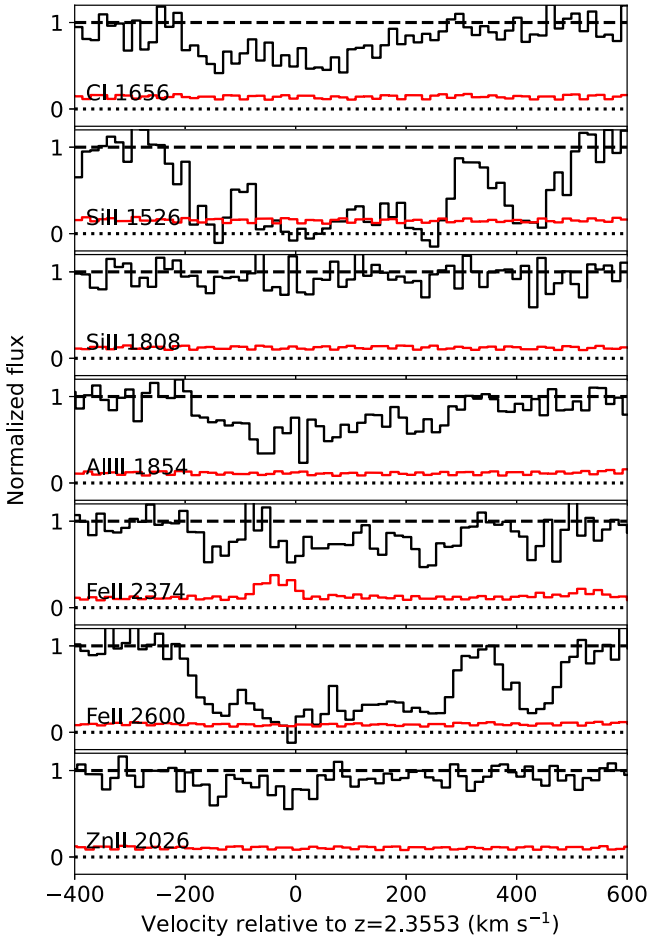

Figure 2. A selection of low- and intermediate-ion metal lines associated with the DLA at $z = 2.3553$ toward QSO J1020+2733, detected in the ESI spectrum. The 1σ uncertainty on the ESI spectrum is shown in red. The metal column densities determined from the detected lines, over the velocity range (−350, +500) km s^{-1}, are listed in Table 1. Absorption is seen over a velocity range of ≈700 km s^{-1}, with $\Delta v_{90} = 480 \pm 50$ km s^{-1}, measured from the Zn IIλ2026 transition.

and in particular the observed damping wings (e.g., A. M. Wolfe et al. 2005; B. T. Draine 2011), we obtain an H I column density of $(5.0 \pm 1.7) \times 10^{20}$ cm^{-2}, i.e., $\log[N_{\rm H\,I}/{\rm cm}^{-2}] = 20.70 \pm 0.15$.

The ESI spectrum shows absorption at $z = 2.3553$ from a wide range of metal lines (see Figure 2). We used the apparent optical depth method to measure the metal column densities and element abundances for this DLA; these are listed in Table 1. We obtain a DLA metallicity of [M/H] = +0.28 ± 0.16 from the Zn IIλ2026 absorption line. The uncertainty on this determination is largely driven by uncertainties in the quasar continuum placement in the H I column density estimate. We also obtain high Fe and Si abundances ([Fe/H]= −0.06 ± 0.15 and [Si/H] = −0.13 ± 0.18), consistent with a supersolar metallicity. We note that, curiously, the dust depletion is only [Zn/Fe] ≈ +0.34—relatively low for DLAs at such a high metallicity (e.g., M. Rafelski et al. 2012; A. De Cia et al. 2016). The velocity spread of the metal lines is $\Delta V_{90} = (480 \pm 50)$ km s^{-1}, also from the Zn IIλ2026 line; this is one of the largest ΔV_{90} values ever measured in a DLA (e.g., M. Neeleman et al. 2013).

Our ALMA spectral cube revealed a high-significance detection of CO(3–2) emission in the field of the $z = 2.3553$ DLA. Figure 3(A) shows the velocity-integrated ALMA

Table 1
Properties of the $z = 2.3553$ DLA

DLA J1020+2733	
R.A. (J2000)	10:20:29.88
decl. (J2000)	+27:33:28.66
Redshift	2.3553
$\log(N(\mathrm{H\ I})/\mathrm{cm}^{-2})$	20.70 ± 0.15
[M/H]	+0.28 ± 0.16
ΔV_{90} (km s^{-1})	480 ± 50
$\log(N(\mathrm{C\ IV})/\mathrm{cm}^{-2})$	>15.37
$\log(N(\mathrm{Al\ II})/\mathrm{cm}^{-2})$	>14.16
$\log(N(\mathrm{Al\ III})/\mathrm{cm}^{-2})$	13.96 ± 0.03
$\log(N(\mathrm{Si\ II})/\mathrm{cm}^{-2})$	15.79 ± 0.11
$\log(N(\mathrm{Si\ IV})/\mathrm{cm}^{-2})$	>14.78
$\log(N(\mathrm{Fe\ II})/\mathrm{cm}^{-2})$	14.95 ± 0.02
$\log(N(\mathrm{Zn\ II})/\mathrm{cm}^{-2})$	13.59 ± 0.06

Note. The metallicity [M/H] is based on the Zn IIλ2026 line. Note that we have not included an estimate of the C I column density, as the C Iλ1656 line is blended with a complex of C I* and C I** lines at the ESI spectral resolution.

CO(3–2) image of the field. The CO(3–2) emission peak is at R.A. $= 10^{\mathrm{h}}20^{\mathrm{m}}29\overset{\mathrm{s}}{.}7756$, decl. $= +27°33'27\overset{''}{.}28$. While the emission appears to be marginally spatially resolved along the east–west direction, the integrated flux density obtained by fitting a 2D Gaussian to the emission region is consistent with the peak flux density. The H I-selected galaxy, DLA1020+2733g, lies at an impact parameter of $\approx 1\overset{''}{.}96 \pm 0\overset{''}{.}02$, i.e., 16.1 ± 0.2 kpc at $z = 2.3553$, southwest of the QSO location.

Figure 3(B) shows the ALMA CO(3–2) spectrum, obtained by taking a cut through the CO cube at the location of the peak in the moment-0 image of Figure 3(A). The CO(3–2) emission has a large FWHM, ≈ 500 km s^{-1}. The galaxy has a redshift of $z_{\mathrm{gal}} = 2.3568$, obtained from a single-Gaussian fit to the CO(3–2) spectrum of Figure 3(B); we will use this as the galaxy redshift in the subsequent analysis. We obtain a velocity-integrated CO(3–2) line flux density of (1.145 ± 0.059) Jy km s^{-1}, implying a CO(3–2) line luminosity of $L'_{\mathrm{CO(3-2)}} = (3.34 \pm 0.17) \times 10^{10}$ K km s^{-1} pc^2.

Our ALMA 104 GHz continuum image of the field of QSO J1020+2733 shows clear emission coincident with DLA1020+2733g (see Figure 4). The continuum emission from the H I-selected galaxy appears extended in the direction of the QSO location. The low impact parameter, ≈ 16 kpc, of the galaxy implies that we cannot rule out the possibility that the extended continuum emission is due to blending of the emission from the galaxy and the QSO. However, we also cannot formally rule out the possibility that the H I-selected galaxy is solely responsible for the observed extended continuum emission. To measure the flux density of the galaxy, we fitted the continuum emission with a 1-component 2D Gaussian model using the CASA task IMFIT. This yielded a 104 GHz continuum flux density of $(128 \pm 29)\ \mu$Jy for DLA1020+2733g. The location of the peak of the continuum emission obtained from the Gaussian fit (indicated by the plus sign in Figure 4) is in agreement with that of the CO(3–2) emission peak. We note that the measured 104 GHz continuum flux density should be considered an upper limit to the flux density of DLA1020+2733g as some of the emission may arise from the QSO.

Finally, our VLA spectral cube yielded a clear detection of CO(1–0) emission from DLA1020+2733g. Figure 5(A) shows the velocity-integrated VLA CO(1–0) image of the galaxy, while Figure 5(B) shows the spectrum obtained by taking a cut through the VLA cube at the peak of the CO(1–0) moment-0 image. The velocity spread of the CO(1–0) line is ≈ 500 km s^{-1}, in excellent agreement with that of the CO(3–2) line. The velocity-integrated CO(1–0) line flux density is (0.248 ± 0.037) Jy km s^{-1}, yielding a CO(1–0) line luminosity of $L'_{\mathrm{CO(1-0)}} = (6.51 \pm 0.97) \times 10^{10}$ K km s^{-1} pc^2. No continuum emission was detected from the DLA galaxy in the VLA 35 GHz continuum image. Table 2 lists the emission properties of DLA1020+2733g.

4. Discussion

Our VLA detection of CO(1–0) emission allows a direct estimate of the molecular gas mass of DLA1020+2733g without any assumptions about the CO excitation. Assuming a CO-to-H_2 conversion factor of $\alpha_{\mathrm{CO}} = 4.36\ M_\odot$ (K km s^{-1} pc^2)$^{-1}$, applicable to main-sequence galaxies of solar metallicity (e.g., A. D. Bolatto et al. 2013; L. J. Tacconi et al. 2020), we obtain $M_{\mathrm{mol}} = (2.84 \pm 0.42) \times (\alpha_{\mathrm{CO}}/4.36) \times 10^{11}\ M_\odot$. This is the largest molecular gas mass ever measured in an H I-selected galaxy (e.g., C. Péroux et al. 2019; N. Kanekar et al. 2020; B. Kaur et al. 2022a).

The measured 104 GHz (i.e., rest frame ≈ 349 GHz) flux density of DLA1020+2733g can be used to determine the total star formation rate (SFR) of the H I-selected galaxy. For this, we assume a dust temperature of ≈ 35 K and an emissivity of $\beta = 1.5$ and then fit a modified blackbody spectrum to the measured rest-frame 349 GHz flux density (e.g., M. Neeleman et al. 2018). Using the integrated continuum flux density of $S_{104\mathrm{GHz}} = 128\ \mu$Jy yields a total infrared (TIR) luminosity between 8 and 1000 μm of $\approx 3 \times 10^{12} L_\odot$. Using the correlation between the TIR luminosity and the SFR (R. C. Kennicutt & N. J. Evans 2012) then gives an SFR of $\approx 400\ M_\odot$ yr^{-1} for DLA1020+2733g. The uncertainty on the SFR estimate is high as it is based on continuum flux densities measured at a rest-frame frequency of ≈ 349 GHz, far away from the peak frequency of the dust continuum emission, and thus depends strongly on the assumed values of β and the dust temperature. Further, we cannot formally rule out the possibility that the detected 104 GHz continuum emission contains a contribution from the QSO. Our SFR estimate from the 104 GHz image should hence be considered an upper limit to the SFR of DLA1020+2733g.

The ratio of the above estimates of the molecular gas mass and the SFR yields a molecular gas depletion timescale of $\tau_{\mathrm{dep}} \gtrsim 0.6$ Gyr. This is higher than the typical molecular gas depletion timescale of galaxies on the main sequence at $z \gtrsim 2$ (≈ 0.2 Gyr; L. J. Tacconi et al. 2020), indicating that DLA1020+2733g has a relatively low star formation efficiency for its molecular gas mass. We note that similarly high gas depletion timescales have been found in three other H I-selected galaxies at $z > 2$: DLA1228-113g at $z \approx 2.193$ (≈ 1.1 Gyr; M. Neeleman et al. 2018; B. Kaur et al. 2022a), DLA0918+1636g at $z \approx 2.5832$ (≈ 0.5 Gyr; J. P. U. Fynbo et al. 2018; B. Kaur et al. 2022a), and DLA0817+1351g at $z \approx 4.258$ (≈ 0.8 Gyr; M. Neeleman et al. 2020). This suggests that selection by H I-absorption tends to pick out gas-rich galaxies with lower star formation efficiencies than typical main-sequence galaxies at similar redshifts, perhaps due to the lack of bias toward high star formation activity. However, as noted above, the uncertainties in these SFR estimates are fairly high as they

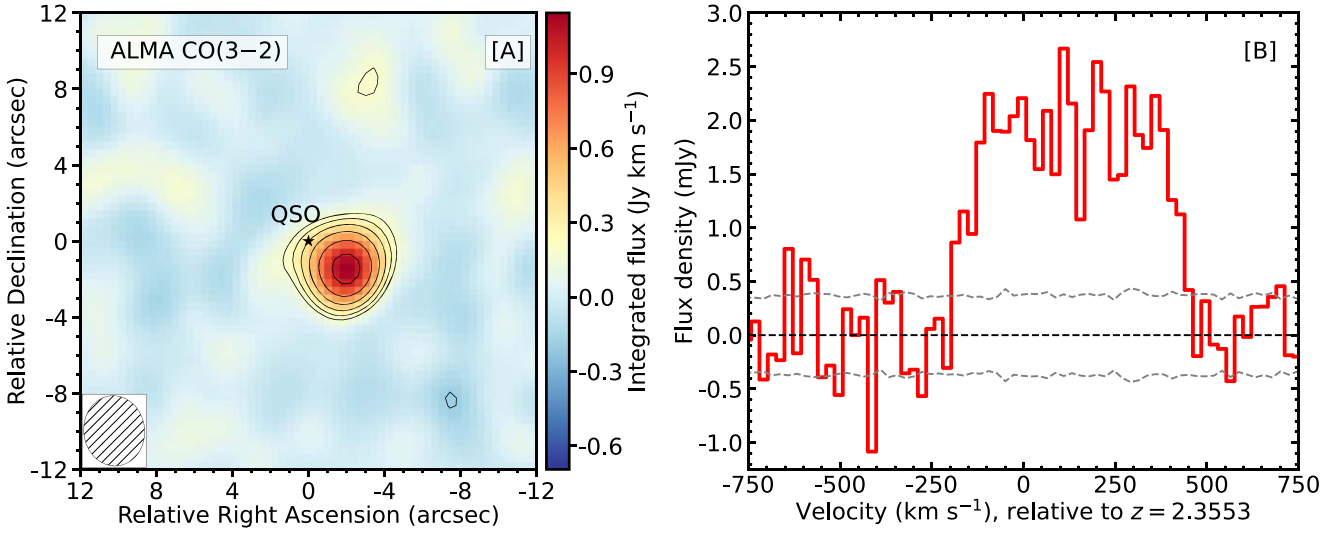

Figure 3. ALMA CO(3–2) emission from the H I-selected galaxy in the field of the $z = 2.3553$ DLA toward QSO J1020+2733. (a) The velocity-integrated ALMA CO(3–2) image of DLA1020+2733g. The contours are at $(-3.0, 3.0, 4.2, 6, 8.5, 12, 17.0) \times \sigma$ significance, with dashed negative contours. The axes are relative to the QSO position, indicated by the black star. (b) The ALMA CO(3–2) emission spectrum of DLA1020+2733g, obtained by taking a cut through the CO cube at the location of the peak in [A]. The dashed gray curves indicate the $\pm 1\sigma$ error on the spectrum.

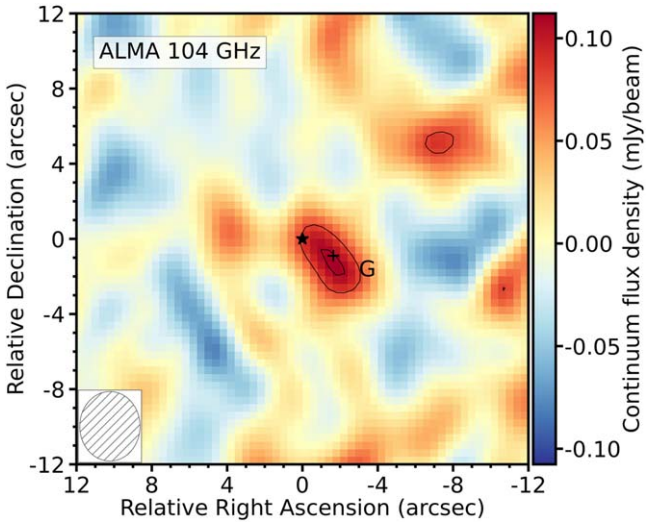

Figure 4. ALMA 104 GHz continuum image of the field of the $z = 2.3553$ DLA toward QSO J1020+2733. The location of the H I-selected galaxy DLA1020+2733g is indicated by the black plus, marked as "G." The contours are at (3.0, 4.0) $\times$ σ significance, where $\sigma = 27$ μJy is the rms noise on the continuum image. We note that there are no negative contours at $\leqslant -3\sigma$ significance in the image. The axes are relative to the QSO position, indicated by the black star.

are based on flux densities in the long wavelength tail of the dust continuum emission.

The above estimates of molecular gas mass and depletion timescale assume $\alpha_{\rm CO} = 4.36\,M_\odot$ $({\rm K\,km\,s^{-1}\,pc^2})^{-1}$. If DLA1020+2733g has a lower CO-to-H_2 conversion factor, $\alpha_{\rm CO} \approx 1\,M_\odot$ $({\rm K\,km\,s^{-1}\,pc^2})^{-1}$, the molecular gas mass and depletion timescale would each be lower by a factor of $\approx$4.5. However, such low $\alpha_{\rm CO}$ values are applicable in starburst galaxies, which have far shorter molecular gas depletion timescales, $<$0.1 Gyr (e.g., L. J. Tacconi et al. 2020), than main-sequence galaxies. For $\alpha_{\rm CO} \approx 1\,M_\odot$ $({\rm K\,km\,s^{-1}\,pc^2})^{-1}$, we would obtain $\tau_{\rm dep} \approx 0.14$ Gyr, similar to that of main-sequence galaxies at $z \approx 2.3$ (e.g., L. J. Tacconi et al. 2020). This relatively long molecular gas depletion timescale makes it unlikely that DLA1020+2733g is a starburst galaxy with a low value of $\alpha_{\rm CO}$. We hence conclude that $\alpha_{\rm CO} \approx 4.36\,M_\odot$ $({\rm K\,km\,s^{-1}\,pc^2})^{-1}$ is likely to apply to the $z = 2.3568$ H I-selected galaxy and that our estimates of $M_{\rm mol} = (2.84 \pm 0.42) \times 10^{11}\,M_\odot$ and $\tau_{\rm dep} \approx 0.6$ Gyr are likely to be reliable. In passing, using a metallicity-dependent CO-to-H_2 conversion factor and the DLA metallicity of $+0.28 \pm 0.16$ yields $\alpha_{\rm CO} \approx 3.5\,M_\odot$ $({\rm K\,km\,s^{-1}\,pc^2})^{-1}$ (e.g., A. D. Bolatto et al. 2013). Using this value of $\alpha_{\rm CO}$, the inferred molecular gas mass is consistent with our estimate based on $\alpha_{\rm CO} = 4.36\,M_\odot$ $({\rm K\,km\,s^{-1}\,pc^2})^{-1}$.

Figure 6 shows a comparison between the velocity profiles of the CO(3–2) emission, the CO(1–0) emission, and a low-ionization metal absorption line (Fe IIλ2600) identified in the ESI spectrum. We note that the absorption arises at a transverse distance of $\approx$16 kpc from DLA1020+2733g. Given this, it is remarkable that the absorption and emission lines show very similar velocity extents, extending over $\approx$700 km s^{-1}. However, the centroids of the CO emission from DLA1020+2733g are offset from the centroid of the Fe IIλ2600 line by $\approx$134 km s^{-1}.

The ratio of the luminosities in the CO(3–2) and CO(1–0) lines allows us to determine the excitation of the $J = 3$ rotational level, r_{31}. We obtain $r_{31} \equiv L_{\rm CO(3-2)}/L_{\rm CO(1-0)} = 0.513 \pm 0.081$, indicating subthermal excitation of the $J = 3$ level (albeit a higher excitation than in the disk of the Milky Way; e.g., D. J. Fixsen et al. 1999). Our estimate is in excellent agreement with the median value of $r_{31} \approx 0.55$ in galaxies near the main sequence at $z \approx$ 0–3 (e.g., E. Daddi et al. 2015; L. J. Tacconi et al. 2020). Earlier studies of massive H I-selected galaxies, as well as massive main-sequence galaxies, at $z \gtrsim 2$ have yielded near-thermal excitation of the $J = 3$ level, $r_{31} \approx 1$ (A. D. Bolatto et al. 2015; K. Henrìquez-Brocal et al. 2022; B. Kaur et al. 2022a). This is the first case of definite subthermal excitation of the $J = 3$ level in an H I-selected galaxy at $z > 2$. B. Kaur et al. (2022a) noted that the near-thermal excitation of the $J = 3$ rotational level in massive galaxies at $z > 2$ appears to be associated with a high SFR surface density in these galaxies (see also L. A. Boogaard et al 2020), as also suggested by theoretical models (e.g., D. Narayanan & M. R. Krumholz 2014). This suggests that DLA1020+2733g may

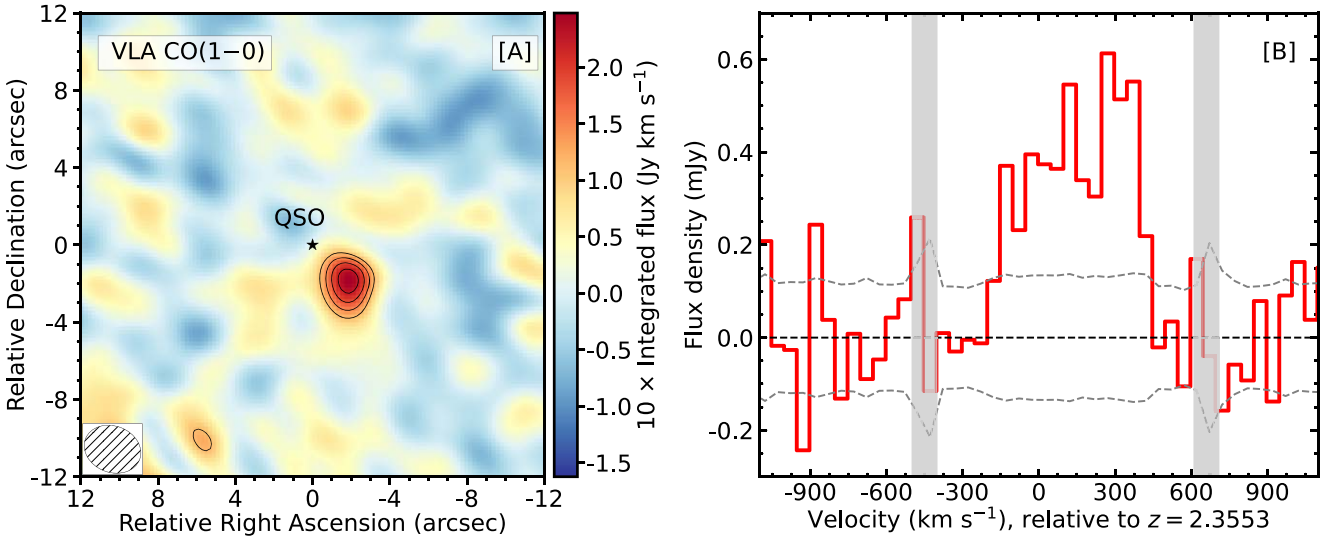

Figure 5. VLA CO(1–0) emission from the H I-selected galaxy in the field of the $z = 2.3553$ DLA toward QSO J1020+2733. (a) The velocity-integrated VLA CO(1–0) image of DLA1020+2733g. The contours are at (3.0, 4.0, 5.0, 6.0) × σ significance. We note that there are no negative contours at $\leqslant -3\sigma$ significance in the image. The axes are relative to the QSO position, indicated by the black star. (b) The VLA CO(1–0) emission spectrum of DLA1020+2733g, obtained by taking a cut through the CO cube at the location of the peak in (a). The gray bands represent the edges of the digital subbands of the WIDAR correlator. The dashed gray curves indicate the $\pm 1\sigma$ error on the spectrum.

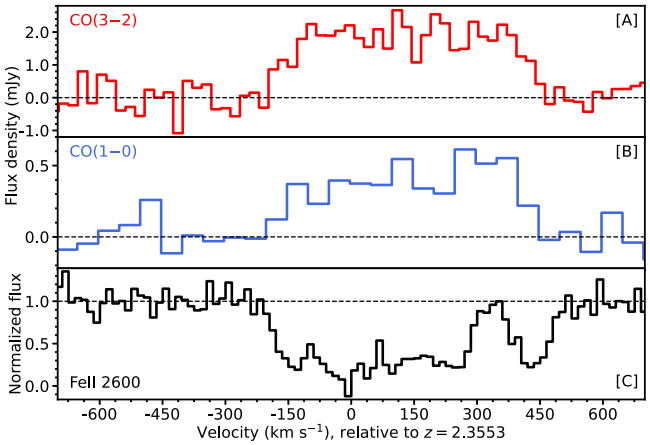

Figure 6. A comparison between the velocity profiles of (a) the CO(3–2) emission and (b) the CO(1–0) emission detected from DLA1020+2733g, with that of [C] the low-ionization metal absorption line, Fe IIλ2600. The velocity scale is relative to the DLA redshift, $z = 2.3553$. The velocity extent of the absorption and emission are seen to be in remarkable agreement.

have a relatively extended molecular disk, yielding a low SFR surface density and hence a lower excitation of the mid-J rotational levels.

The large-velocity FWHMs ($\approx$500 km s^{-1}) of the CO(1–0) and CO(3–2) lines in DLA1020+2733g are similar to the FWHMs ($\approx$600 km s^{-1}) of these lines in the H I-selected galaxy DLA1228-113g at $z \approx 2.193$ (M. Neeleman et al. 2018; B. Kaur et al. 2022a). Both galaxies also have large molecular gas masses and high gas depletion timescales, suggesting that they are relatively gas-rich systems with a low star formation efficiency (although DLA1228-113g shows near-thermal excitation of the $J = 3$ rotational level and a high SFR surface density). It thus appears likely that, similar to DLA1228-113g (B. Kaur et al. 2024), DLA1020+2733g may also be a cold, rotating-disk galaxy. The high CO(3–2) integrated flux density implies that it should be straightforward to test this hypothesis via a high-resolution ALMA mapping study.

Table 2
Emission Properties of the H I-absorption-selected Galaxy DLA1020+2733g

	DLA1020+2733g
R.A. (J2000)	10:20:29.775
decl. (J2000)	+27:33:27.28
Redshift	2.3568
Impact parameter (kpc)	16.1 ± 0.2
$L'_{\rm CO(3-2)}$ (K km s^{-1} pc^2)	(3.34 ± 0.17) × 10^{10}
$L'_{\rm CO(1-0)}$ (K km s^{-1} pc^2)	(6.51 ± 0.97) × 10^{10}
$S_{\rm cont}$ (μJy), at $\nu_{\rm obs} = 104$ GHz	(128 ± 29)
$M_{\rm mol}$ ($M_\odot$)	(2.84 ± 0.42) × 10^{11}
SFR ($M_\odot$ yr^{-1})	$\lesssim$400
$t_{\rm dep}$ (Gyr)	$\gtrsim$0.6
r_{31}	(0.513 ± 0.081)

Note. The estimates of the molecular gas mass and the molecular gas depletion timescale assume $\alpha_{\rm CO} \approx 4.36\, M_\odot$ (K km s^{-1} pc^2)$^{-1}$.

5. Summary

We have used the VLA and ALMA to identify, via its CO(1–0) and CO(3–2) emission, a $z = 2.3568$ H I-selected galaxy in the field of the $z = 2.3553$ DLA toward QSO J1020+2733 at an impact parameter of $\approx$16 kpc. The galaxy, DLA1020+2733g, has a molecular gas mass of $M_{\rm mol} = (2.84 \pm 0.42) \times 10^{11} \times (\alpha_{\rm CO}/4.36)\, M_\odot$, the largest measured so far in an H I-selected galaxy. The CO(3–2) and CO(1–0) lines are extended over a velocity range of $f \approx 700$ km s^{-1}, in remarkable agreement with the extent of the low-ionization metal absorption lines detected in our Keck ESI spectrum toward the QSO. The velocity spread of the metal absorption lines is $\Delta V_{90} = 480 \pm 50$ km s^{-1}, one of the highest ever measured in a DLA. The ratio of CO(3–2) and CO(1–0) line luminosities yields an excitation of $r_{31} = 0.513 \pm 0.081$ for the $J = 3$ rotational level; this is the first case of clear subthermal excitation of the $J = 3$ level for a massive galaxy at $z > 2$,

suggesting that the DLA galaxy is likely to have a low SFR surface density. The ALMA-detected rest-frame 349 GHz dust continuum yields an SFR of $\lesssim 400\,M_{\odot}\,\mathrm{yr}^{-1}$ for DLA1020+2733g and a molecular gas depletion timescale of $\gtrsim 0.6$ Gyr. This is longer than the typical molecular gas depletion timescales in main-sequence galaxies at $z \approx 2.3$, suggesting that DLA1020+2733g has a relatively low star formation efficiency for its molecular gas mass. We obtain an H I column density of $(5.0 \pm 1.7) \times 10^{20}\,\mathrm{cm}^{-2}$ and a metallicity of $[\mathrm{Z/H}] = +0.28 \pm 0.16$ for the $z = 2.3553$ DLA, continuing the trend of the highest-metallicity DLAs arising in or around massive galaxies at $z \approx 2$. The subthermal CO excitation, large velocity spread, and long gas depletion timescale suggest that DLA1020+2733g is likely to be a cold, rotating-disk galaxy.

Acknowledgments

We thank an anonymous referee for useful comments on an earlier draft of this Letter. B.K. and N.K. acknowledge support from the Department of Atomic Energy under project 12-R&D-TFR-5.02-0700; N.K. also acknowledges support from the Science and Engineering Research Board of the Department of Science and Technology via a J. C. Bose Fellowship (JCB/2023/000030). This material is based upon work supported by the National Science Foundation under grant No. 2107989. ALMA is a partnership of ESO (representing its member states), NSF (USA) and NINS (Japan), together with NRC (Canada), NSC and ASIAA (Taiwan), and KASI (Republic of Korea), in cooperation with the Republic of Chile. The Joint ALMA Observatory is operated by ESO, AUI/NRAO, and NAOJ. The National Radio Astronomy Observatory is a facility of the National Science Foundation operated under cooperative agreement by Associated Universities, Inc. The data reported in this Letter are available through the ALMA archive (https://almascience.nrao.edu/alma-data/archive) with project code ADS/JAO.ALMA #2023.1.01415.S. Some of the data presented herein were obtained at Keck Observatory, which is a private 501(c)3 nonprofit organization operated as a scientific partnership among the California Institute of Technology, the University of California, and the National Aeronautics and Space Administration. The Observatory was made possible by the generous financial support of the W. M. Keck Foundation.

Facilities: ALMA, VLA, Keck: II(ESI).

Software: CASA (CASA Team 2022); GDL (A. Coulais et al. 2010); CALR (A. Chowdhury 2021).

ORCID iDs

B. Kaur https://orcid.org/0000-0002-1372-0686
N. Kanekar https://orcid.org/0000-0002-9757-7206
M. Neeleman https://orcid.org/0000-0002-9838-8191
Y. Zhu https://orcid.org/0000-0003-3307-7525
J. X. Prochaska https://orcid.org/0000-0002-7738-6875
M. Rafelski https://orcid.org/0000-0002-9946-4731

References

Arinyo-i-Prats, A., Mas-Ribas, L., Miralda-Escudé, J., Pérez-Ràfols, I., & Noterdaeme, P. 2018, MNRAS, 481, 3921
Balashev, S. A., Klimenko, V. V., Noterdaeme, P., et al. 2019, MNRAS, 490, 2668
Becker, G. D., Pettini, M., Rafelski, M., et al. 2019, ApJ, 883, 163
Bolatto, A. D., Warren, S. R., Leroy, A. K., et al. 2015, ApJ, 809, 175
Bolatto, A. D., Wolfire, M., & Leroy, A. K. 2013, ARA&A, 51, 207
Boogaard, L. A., van der Werf, P., Weiss, A., et al. 2020, ApJ, 902, 109
Briggs, D. S. 1995, AAS Meeting Abstracts, 187, 112.02
CASA Team 2022, PASP, 134, 114501
Chowdhury, A. 2021, calR: Robust Calibration in CASA, v3.3.1, Zenodo, doi:10.5281/zenodo.4723688
Chowdhury, A., Kanekar, N., & Chengalur, J. N. 2022, ApJ, 937, 103
Chowdhury, A., Kanekar, N., Chengalur, J. N., Sethi, S., & Dwarakanath, K. S. 2020, Natur, 586, 369
Combes, F., & Gupta, N. 2024, A&A, 683, A20
Coulais, A., Schellens, M., Gales, J., et al. 2010, in ASP Conf. Ser. 434, Astronomical Data Analysis Software and Systems XIX, ed. Y. Mizumoto, K. I. Morita, & M. Ohishi (San Francisco, CA: ASP), 187
Daddi, E., Dannerbauer, H., Liu, D., et al. 2015, A&A, 577, A46
De Cia, A., Ledoux, C., Mattsson, L., et al. 2016, A&A, 596, A97
Draine, B. T. 2011, Physics of the Interstellar and Intergalactic Medium (Princeton, NJ: Princeton Univ. Press)
Fixsen, D. J., Bennett, C. L., & Mather, J. C. 1999, ApJ, 526, 207
Fumagalli, M., O'Meara, J. M., Prochaska, J. X., Kanekar, N., & Wolfe, A. M. 2014, MNRAS, 444, 1282
Fynbo, J. P. U., Heintz, K. E., Neeleman, M., et al. 2018, MNRAS, 479, 2126
Fynbo, J. P. U., Laursen, P., Ledoux, C., et al. 2010, MNRAS, 408, 2128
Henrìquez-Brocal, K., Herrera-Camus, R., Tacconi, L., et al. 2022, A&A, 657, L15
Horne, K. 1986, PASP, 98, 609
Hunter, T. R., Indebetouw, R., Brogan, C. L., et al. 2023, PASP, 135, 074501
Jones, A., Noll, S., Kausch, W., Szyszka, C., & Kimeswenger, S. 2013, A&A, 560, A91
Kanekar, N., Prochaska, J., Neeleman, M., et al. 2020, ApJL, 901, L5
Kanekar, N., Prochaska, J. X., Christensen, L., et al. 2018, ApJL, 856, L23
Kanekar, N., Prochaska, J. X., Smette, A., et al. 2014, MNRAS, 438, 2131
Kaur, B., Kanekar, N., Neeleman, M., et al. 2024, ApJL, 971, L33
Kaur, B., Kanekar, N., Rafelski, M., et al. 2021, ApJ, 921, 68
Kaur, B., Kanekar, N., Rafelski, M., et al. 2022a, ApJL, 933, L42
Kaur, B., Kanekar, N., Revalski, M., et al. 2022b, ApJ, 934, 87
Kelson, D. D. 2003, PASP, 115, 688
Kennicutt, R. C., & Evans, N. J. 2012, ARA&A, 50, 531
Klitsch, A., Zwaan, M. A., Péroux, C., et al. 2019, MNRAS, 482, L65
Krogager, J. K., Møller, P., Fynbo, J. P. U., & Noterdaeme, P. 2017, MNRAS, 469, 2959
Kulkarni, V. P., Hill, J. M., Schneider, G., et al. 2000, ApJ, 536, 36
Lofthouse, E. K., Fumagalli, M., Fossati, M., et al. 2023, MNRAS, 518, 305
Madau, P., & Dickinson, M. 2014, ARA&A, 52, 415
Mas-Ribas, L., Miralda-Escudé, J., Pérez-Ràfols, I., et al. 2017, ApJ, 846, 4
Møller, P., Christensen, L., Zwaan, M. A., et al. 2018, MNRAS, 474, 4039
Møller, P., Fynbo, J. P. U., & Fall, S. M. 2004, A&A, 422, L33
Møller, P., Warren, S. J., Fall, S. M., Fynbo, J. U., & Jakobsen, P. 2002, ApJ, 574, 51
Narayanan, D., & Krumholz, M. R. 2014, MNRAS, 442, 1411
Neeleman, M., Kanekar, N., Prochaska, J. X., Rafelski, M. A., & Carilli, C. L. 2019, ApJL, 870, L19
Neeleman, M., Kanekar, N., Prochaska, J. X., Rafelski, M. A., & Kahinga, L. A. 2025, ApJ, in press
Neeleman, M., Kanekar, N., Prochaska, J. X., et al. 2017, Sci, 355, 1285
Neeleman, M., Kanekar, N., Prochaska, J. X., et al. 2018, ApJL, 856, L12
Neeleman, M., Prochaska, J. X., Kanekar, N., & Rafelski, M. 2020, Natur, 581, 269
Neeleman, M., Prochaska, J. X., & Wolfe, A. M. 2015, ApJ, 800, 7
Neeleman, M., Wolfe, A. M., Prochaska, J. X., & Rafelski, M. 2013, ApJ, 769, 54
Noll, S., Kausch, W., Barden, M., et al. 2012, A&A, 543, A92
Noterdaeme, P., Ledoux, C., Petitjean, P., & Srianand, R. 2008, A&A, 481, 327
Oyarzún, G. A., Rafelski, M., Kanekar, N., et al. 2024, ApJ, 962, 72
Péroux, C., Bouché, N., Kulkarni, V. P., York, D. G., & Vladilo, G. 2012, MNRAS, 419, 3060
Péroux, C., Zwaan, M. A., Klitsch, A., et al. 2019, MNRAS, 485, 1595
Prochaska, J. X., Neeleman, M., Kanekar, N., & Rafelski, M. 2019, ApJL, 886, L35
Rafelski, M., Neeleman, M., Fumagalli, M., Wolfe, A. M., & Prochaska, J. X. 2014, ApJL, 782, L29

Rafelski, M., Wolfe, A. M., Prochaska, J. X., Neeleman, M., & Mendez, A. J. 2012, ApJ, 755, 89
Rhodin, N. H. P., Krogager, J. K., Christensen, L., et al. 2021, MNRAS, 506, 546
Sheinis, A. I., Bolte, M., Epps, H. W., et al. 2002, PASP, 114, 851
Tacconi, L. J., Genzel, R., & Sternberg, A. 2020, ARA&A, 58, 157
Wang, W.-H., Kanekar, N., & Prochaska, J. X. 2015, MNRAS, 448, 2832
Wolfe, A. M., Gawiser, E., & Prochaska, J. X. 2005, ARA&A, 43, 861
Wolfe, A. M., Turnshek, D. A., Smith, H. E., & Cohen, R. D. 1986, ApJS, 61, 249